



# Heat transfer enhancement of turbulent channel flow using dual self-oscillating inverted flags: Staggered and side-by-side configurations

Yujia Chen, Yuelong Yu, Di Peng, Yingzheng Liu\*

Key Lab of Education Ministry for Power Machinery and Engineering, School of Mechanical Engineering, Shanghai Jiao Tong University, 800 Dongchuan Road, Shanghai 200240, China  
Gas Turbine Research Institute, Shanghai Jiao Tong University, 800 Dongchuan Road, Shanghai 200240, China

## ARTICLE INFO

### Article history:

Received 27 December 2018

Received in revised form 5 March 2019

Accepted 8 March 2019

### Keywords:

Inverted flag  
Heat transfer  
Side-by-side flags  
Staggered flags  
TSP

## ABSTRACT

This study experimentally determined the flapping dynamics of dual self-oscillating inverted flags placed inside turbulent channel flows in side-by-side and staggered configurations and their ability to enhance wall heat removal. Three clearance-distance to channel-width ratios ( $G_c/W = 0.19, 0.31, \text{ and } 0.5$ ) and three streamwise-distance to channel-width ratios ( $G_y/W = 0, 2, \text{ and } 4$ ) were used to examine distinct flag behaviors. A single flag mounted to the heated wall with various gap clearances was chosen as the benchmark. The flags' time-varying motions were recorded by a high-speed camera system. Three dynamic regimes were identified on the basis of the flags' dimensionless stiffness and the channel flow's Reynolds number: the biased mode, the flapping mode, and the deflected mode. Temperature sensitive paint (TSP) measurements demonstrated that the best cooling enhancement, with a local Nusselt number ratio of over 1.6, was achieved for the single flag system at  $G_c/W = 0.19$ . Adding another inverted flag to the side-by-side configuration at  $G_c/W = 0.19$  further enhanced the heat removal performance on both channel walls, and the flapping period increased by nearly 50%. However, placing two side-by-side flags close to each other ( $G_c/W = 0.31$ ) led to chaotic flapping motions, resulting in diminutive augmentation in heat transfer and an appreciable penalty in pressure drop. In the staggered configuration at  $G_y/W = 2$  and 4, the two inverted flags synchronously flapped with a stable phase difference, and the flapping periods were similar to those of the single flag. The peak Nusselt number ratio was 1.9 for  $G_y/W = 2$ , which was attributed to the concerted influence of the staggered inverted flags. The system with staggered flags placed close to the heated wall had a higher thermal enhancement factor than the system with flags mounted in tandem along the channel centerline.

© 2019 Elsevier Ltd. All rights reserved.

## 1. Introduction

The heat transfer of channel flow plays an important role in industry applications, e.g., in gas turbines and heat exchangers, and can be considerably intensified by various turbulence enhancement mechanisms (e.g., ribs, pin fins, protrusions, and dimples [1–4]). However, such strategies significantly deteriorate in turbulent channel flows with low Reynolds numbers ( $\sim 10^4$ ), which are common in electronic products due to their highly limited effective areas and the increased cost of pressure drop. To overcome this issue, active vortex generators, such as piezo fans and magnetic fans [5,6], have been developed, but these depend

on reliable external power supplies. Recent studies have shown [7] that placing a flexible flag in the channel and then forcing it into a self-oscillating motion produces substantial gains in heat transfer in the extended area [8], probably due to the flag's instability and the highly unsteady channel flow behind the flag.

A few preliminary attempts have been made to promote wall heat removal by placing a flag or multiple flags in the channel. For laminar channel flow at a very low Reynolds number ( $Re = 600$ ), two vertically wall-mounted flexible flags [9,10] were forced into self-oscillating motions with a moderate amplitude to flag-length ratio,  $A/L > 0.35$ ; the numerical results suggested an optimized heat transfer performance with nearly 100% enhancement in mean heat flux. However, recent experimental attempts [11] have indicated that such intense flapping is hard to generate in a turbulent channel flow. A computational study of laminar channel flow at  $Re < 800$  [12] showed that the flow-induced vibra-

\* Corresponding author at: Key Lab of Education Ministry for Power Machinery and Engineering, School of Mechanical Engineering, Shanghai Jiao Tong University, 800 Dongchuan Road, Shanghai 200240, China.

E-mail address: [yqliu@sjtu.edu.cn](mailto:yqliu@sjtu.edu.cn) (Y. Liu).

## Nomenclature

$A$	flapping amplitude [m]	$W$	width of the channel [m]
$B$	flexural rigidity [NA · m]	$x$	transverse direction [m]
$C^*$	length to channel width ratio $C^* = L/W$	$y$	streamwise direction [m]
$E$	young's modulus of the inverted flag [GPa]	$z$	spanwise direction [m]
$F$	friction factor	$X^*$	normalized transverse coordinate
$f$	flapping frequency of the inverted flag [Hz]	$Y^*$	normalized streamwise coordinate
$f_T$	TSP function	$Z^*$	normalized spanwise coordinate
$G_c$	gap clearance between the flag and wall [m]		
$G_x$	separation distance between two flags in the transverse (x) direction [m]	<i>Greek symbols</i>	
$G_y$	separation distance between two flags in the streamwise (y) direction [m]	$\delta_{99}$	thickness of the turbulent boundary layer [m]
$H_c$	height of the wind channel [m]	$\eta$	thermal enhancement factor
$H$	height (or span) of the inverted flag [m]	$\nu$	Poisson's ratio of the inverted flag
$h$	thickness of the inverted flag [m]	$\lambda$	thermal conductivity of the air [ $W \cdot m^{-1} \cdot K^{-1}$ ]
$I$	luminescence intensity of the TSP	$\rho_f$	fluid density [ $kg \cdot m^{-3}$ ]
$K_B$	dimensionless bending stiffness	$\rho_s$	density of the inverted flag [ $kg \cdot m^{-3}$ ]
$L$	length of the inverted flag [m]		
$L_p$	distance between two pressure taps [m]	<i>Subscripts</i>	
$Nu$	Nusselt number	$0$	smooth channel
$Nu^*$	Nusselt number ratio	$ref$	reference
$P$	electronic power applied to the heating foil [W]	$air, in$	inlet air
$\Delta p$	pressure drop between two pressure taps [Pa]		
$R$	results calculated from variables	<i>Abbreviation</i>	
$Re_W$	Reynolds number (based on the width of the channel)	CCD	charge coupled device
$S$	area of the heating foil [ $m^2$ ]	CMOS	complementary metal oxide semiconductor
$T$	temperature [K]	FFT	fast fourier transform
$t^*$	dimensionless time	TSP	temperature sensitive paint
$\Delta t^*$	dimensionless flapping period	TR-PIV	time-resolved particle image velocimetry
$U_0$	free stream velocity [ $m \cdot s^{-1}$ ]	UV-LED	ultraviolet light-emitting diode
$V$	measured variables		

tion of a conventional flag (clamped at the leading edge and free at the trailing edge) resulted in an appreciable convective heat transfer augmentation of over 60%. Unfortunately, the extremely soft flag used in the numerical study was nearly unavailable in engineering applications. A real flag in the conventional configuration can be experimentally excited by the channel flow at a high Reynolds number, up to  $10^5$  [13,14]; however, this is challenging for  $Re \leq 10^4$  [15]. A single inverted flag (free at the leading edge and fixed at the trailing edge) with a length to channel-width ratio of  $C^* = 0.5$  was excited to an intense flapping motion at the channel laminar flow ( $Re < 800$ ) by Park et al. [16], who reported heat transfer enhancement of 150%, but with a penalty of nine times the mechanical energy loss. Subsequently, Yu et al. [17] experimentally examined the heat transfer enhancement performance of three inverted flags of different lengths ( $C^* = 0.125, 0.25,$  and  $0.375$ ) in the range of  $Re = 1.2 \times 10^4 - 2.3 \times 10^4$ . They found the local Nusselt number increased by 20% for a short flag ( $C^* = 0.125$ ), and the pressure drop increased by 69%. As the longest flag ( $C^* = 0.375$ ) was in flapping mode, it achieved the best cooling performance, with a remarkable augmentation of up to 70%, but at a substantial cost in pressure drop, which increased by a factor of 3.17. This increase in pressure drop was attributed to the energetic vortex shedding process behind the flag, and was confirmed by the time-resolved particle image velocimetry (TR-PIV) measurement of the unsteady flow [17]. Using tandem flags ( $C^* = 0.25$ ) along the channel centerline, Chen et al. [8] successfully doubled the local Nusselt number for the extended streamwise area, but the total pressure drop still exceeded the smooth channel without flags by a factor of four. In these studies [8,17], the considerable penalty in pressure drop was the result of a large blockage of the long flag

to the high-speed mainstream, which is needed for a flag placed in the channel centerline to generate a large flapping motion and sweep out the thermal boundary layer. It is well established that placing short inverted flags in proximity to a heated wall introduces strong disturbance to the near-wall flow, intensifying wall heat removal at a reduced pressure drop across the entire channel, and that the effective heat transfer enhancement area can be extended by different configurations of the paired flags.

Building on Chen et al. [8], this study quantified the coupling flapping dynamics of dual inverted flags in proximity to the wall and the resultant heat transfer enhancement. Using a single flag as a benchmark, two representative configurations of the paired flags, staggered and side-by-side, were compared. A total of three clearance-distance to channel-width ratios ( $G_c/W = 0.19, 0.31,$  and  $0.5$ ) and three streamwise-distance to channel-width ratios ( $G_y/W = 0, 2,$  and  $4$ ) were varied to examine their distinct behaviors. In the experiment, a high-speed camera was installed to identify the flags' flapping motions; the spatially varying temperature field on the heated wall surface was determined using the temperature sensitive paint (TSP) technique.

## 2. Experimental setup

### 2.1. Flag dynamics measurement apparatus

Fig. 1(a) presents a schematic diagram of the experimental setup to measure the flag flapping dynamics. Two rectangular and flexible inverted flags made of transparent polyethylene terephthalate (density  $\rho_s = 1.38 \times 10^3 kg/m^3$ , Young's modulus  $E = 2.2 GPa$ , and Poisson's ratio  $\nu = 0.39$ ) were set parallel to the

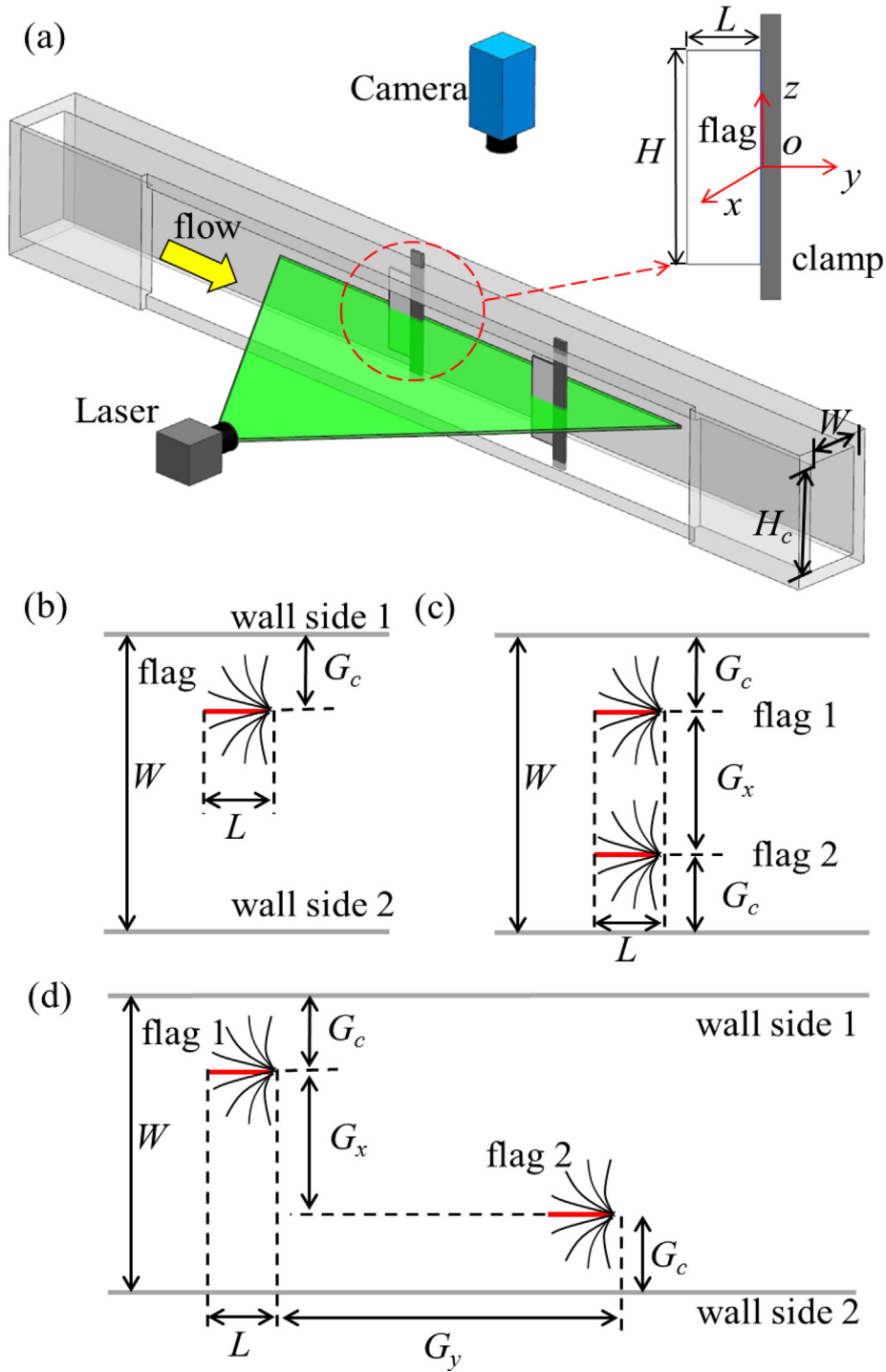


**Fig. 1.** Flag flapping dynamics: (a) schematic diagram of experimental setup; (b) single flag configuration; (c) side-by-side flags configuration; and (d) staggered flags configuration.

flow. The flags shared the same thickness ( $h = 0.025$  mm), height (or span) ( $H = 60$  mm), and length ( $L = 7.5$  mm,  $C^* = 0.19$ ). These dimensions led to a high aspect ratio ( $H/L = 8$ ) that guaranteed two-dimensional flapping motions near the mid-span position. The inverted flag was clamped at its trailing edge with two pieces of carbon fiber plate that were 3 mm in length and 0.5 mm in thickness. The right-hand coordinate origin was situated at the mid-span of the upstream flag trailing edge, and the  $x$ ,  $y$ , and  $z$  axes denoted the transverse, streamwise, and spanwise orientations, respectively. All of the coordinates were normalized by the channel

width  $W$ , i.e.,  $X^* = x/W$ ,  $Y^* = y/W$ , and  $Z^* = z/W$ . The measurements were conducted in a subsonic open-circuit wind tunnel with an 80 mm (height,  $H_c$ )  $\times$  40 mm (width,  $W$ ) cross section that had been previously installed by Chen et al. [8]. The wind tunnel was equipped with a contraction section (contraction ratio 7:1) to straighten the air flow entering the test segment. The top-hatted inlet velocity profile, with a turbulent boundary layer thickness of  $\delta_{99} = 0.25 W$ , was measured by moving the hot-wire probe along the normal-wall ( $x$ ) direction; the turbulence intensity was below 2% for the current free-stream velocity range  $U_0 = 5.8 - 9.4$  m/s

( $Re_w = \rho_f U_0 W / \mu_f$  ranged from  $1.55 \times 10^4$  to  $2.52 \times 10^4$ ). The dimensionless bending stiffness [7]  $K_B = B / \rho_f U_0^2 L^3$ , which characterizes the relative magnitude of the bending force to the fluid inertial force exerted on the flag, ranged from 0.198 to 0.075. Herein,  $\rho_f = 1.2 \text{ kg/m}^3$  denotes the air density (1 atm, 395 K) and  $B = Eh^3 / 12(1 - \nu^2)$  is the flexural rigidity of the flag.

To visualize the flag motions, a 5 W continuous-wave semiconductor laser (532 nm) was used to illuminate the mid-span of the flags, as shown in Fig. 1(a). A 12-bit high-speed CMOS camera (dimax HS4, PCO, USA) was installed on the top of the wind channel to record the flapping dynamics of the inverted flags. The camera was operated at a speed of 2000 fps (the flag flapping frequency,  $f$ , was around 100 Hz for all of the experiments) with a resolution of  $1500 \times 600$  pixels (0.1375 mm/pixel), allowing the instantaneous flag profiles of the two inverted flags to be captured simultaneously. Inspired by the side-by-side and staggered flag systems proposed by Cerdeira et al. [18], Ryu et al. [19], and Huang et al. [20], three configurations were tested, as shown in Fig. 1(b)–(d): (b) a single flag, (c) side-by-side flags, and (d) staggered flags. In Fig. 1,  $G_c$  is the gap clearance between the flag and the wall,  $G_x$  is the separation distance in the transverse ( $x$ ) direction, and  $G_y$  denotes the separation distance in the streamwise ( $y$ ) direction. To improve the clarity of the discussion of the results in following sections, the upper and lower walls in Fig. 1(b)–(d) are marked as wall side 1 and wall side 2, respectively.

2.2. Heat transfer performance measurement apparatus

The heat transfer measurements were conducted in the same wind tunnel. The spatially varying temperature field on the heated wall was quantified using the temperature sensitive paint (TSP) [21] technique. TSP is a molecular temperature sensor consisting of luminescent molecules and a binder. When illuminated by light of a certain wavelength (385 nm in this study), the luminescent molecules in the TSP layer are excited into an unstable elevated energy state, which is susceptible to shifting to a ground state through two mechanisms: thermal deactivation and luminescent deactivation (i.e., luminescence wavelength around 600 nm). As the temperature rises, thermal deactivation increases and luminescent deactivation decreases, leading to attenuated luminescence intensity. The temperature field, accurately indicated by the luminescence intensity, can be determined by examining their relationship, which is generally described by the function  $f_T$  in the following equation:

$$\frac{I_{ref}}{I} = f_T(T, T_{ref}), \tag{1}$$

where  $I_{ref}$  is the luminescence intensity at a specified reference temperature  $T_{ref}$  (usually room temperature) and  $I$  is the luminescence intensity at arbitrary temperature  $T$ . The process for calibrating function  $f_T$  is discussed below.

Fig. 2 shows the schematic diagram of the heat transfer experiment apparatus. To produce the TSP layer, an oxygen-impermeable automobile clearcoat (Dupont ChromClear HC7776S) was used as a binder, and Ru (dpp) (GFS Chemical, Inc.) was selected as the temperature sensor [22–24]. The TSP sensor was dissolved in methanol and mixed with the clearcoat binder. Then, the TSP solution was air-sprayed onto a thin stainless steel plate (500 mm in length, 40 mm in width, and 0.5 mm in thickness), and left for several hours until dry. To provide an adjustable and uniform heat flux, the whole upper surface of the stainless steel plate was covered with a heating foil (0.1 mm thick, Backer Calesco, Sweden). A direct current (DC) source provided continuous and stable electronic power to the heating foil; the electronic power could be measured by the built-in voltmeter and ammeter inside the DC source. A suitable cavity in the upper channel wall (made of Plexiglas) was carefully designed to embed the heated plate so that the flow distortion would be eliminated. A thermal insulation layer (10 mm thick, thermal conductivity  $< 0.025 \text{ W/m}\cdot\text{K}$ ) was used to minimize heat loss from thermal conduction; heat loss through the insulated wall was estimated to be less than 1% of the power input. Eighteen T-type thermocouples were attached to the heating foil to monitor the plate temperature. Their locations in relation to the inverted flags are plotted in Fig. 2. Two additional thermocouples were installed at the channel inlet and outlet to obtain the airflow temperature. The experiments were conducted in a constant-temperature room in which the air conditions and inlet air temperature was kept at around 295 K. All of the temperature signals were simultaneously captured by a data acquisition system (Fluke 2638A, USA). The pressure drop was measured by a manometer placed between the two pressure taps situated on the lower transparent Plexiglas wall (accessible as a light path) at  $Y^* = -3.5$  and 6, respectively. Under excitation by the 385 nm UV-LED (UHP-T-LED-385, Prizmatix), the TSP layer emitted luminescent signals, which were captured by a 14-bit CCD camera (PCO 1600, USA) with a resolution of  $1600 \times 1200$  pixels (0.1837 mm/pixel). The camera lens (Nikon 35 mm  $f/2.8$ ) was equipped with a band-pass filter ( $575 \pm 25 \text{ nm}$ ) to exclude any excitation light from the UV-LED.

The local Nusselt number  $Nu$  is widely used as a dimensionless index to measure cooling performance, and is defined as follows:

$$Nu = \frac{PW}{S\lambda(T - T_{air,in})}, \tag{2}$$

where  $S$  denotes the heating foil area,  $P$  is the power of DC source,  $\lambda$  is the thermal conductivity of air, and  $T$  and  $T_{air,in}$  represent, respectively, the local wall temperature and inlet airflow temperature measured after the heat-balanced state was established. The stainless steel plate was under the dual influence of the electronic heating, with constant power  $P$ , and cold air cooling, which depended on surface temperature  $T$ ; as  $T$  gradually increased, a heat-balanced state was eventually reached when the heating power was equivalent to the heat convection toward the cold air, guaranteeing a fully development of the heat transfer before measurement. The stainless steel plate was deemed to be in the heat-balance state when the maximum variation in temperature measured by every single thermocouple was less than 0.1 K over a 5-min period, with a calculated diversity of 0.045% between the heat input and heat transferred to the cold air. The temperature difference  $T - T_{air,in}$  in the heat-balanced state was maintained at 15–30 K for all of the experimental cases.

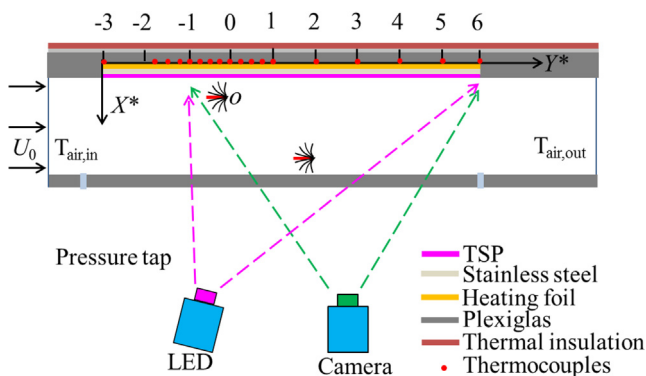


Fig. 2. Schematic diagram of the heat transfer experimental setup.

The TSP measurement procedure and the in-situ calibration process for the function  $f_T$  were performed simultaneously. Firstly, the luminescent intensity distribution  $I_{ref}$  was acquired at room temperature,  $T_{ref}$ . Then, the heat power and the wind tunnel were turned on. After the establishment of the heat-balance state, the image intensity  $I$  captured by the camera and the corresponding temperature value  $T$  measured by the thermocouples were collected simultaneously. Experimental data (scatter points) from all of the successful runs were applied to fit the calibration curve  $f_T$ , shown in Fig. 3, and the deviation between the measurement data and the fitted curve was below 0.2%. The accuracy of the T-type thermocouples was  $\pm 0.5$  K. The uncertainty of the TSP measurement was estimated to be within  $\pm 0.7$  K. Based on the fitted calibration curve and the image intensity distribution,  $I$ , measured on the heated plate, the global temperature distribution  $T$  was accurately determined.

The uncertainty analysis was based on a confidence level of 95% proposed by Moffat [25]. The results,  $R$ , of the experiment are assumed to be calculated from a series of variables,  $V_i$ , as follows:

$$R = R(V_1, V_2, V_3, \dots, V_N). \quad (3)$$

Then, the comprehensive relative uncertainty was determined as follows:

$$\frac{\Delta R}{R} = \left\{ \sum_{i=1}^N \left( \frac{\partial R}{\partial V_i} \times \frac{\Delta V_i}{R} \right)^2 \right\}^{1/2}, \quad (4)$$

where  $\Delta R$  and  $\Delta V_i$  denote the uncertainty in  $R$  and  $V_i$ , respectively. Substituting Eq. (2) into Eq. (4) gave a comprehensive relative uncertainty of the local  $Nu$  as 7%. The Nusselt number ratio [8,17,22]  $Nu^* = Nu/Nu_0$  indicates the magnitude of the enhancement of the heat transfer performance relative to the smooth channel. The  $Nu_0$  at the corresponding Reynolds numbers for the smooth channel without a flag were also measured. To further clarify the heat transfer enhancement performance, the results are presented by  $Nu^*$  below.

### 3. Results and discussion

#### 3.1. Single flag

The flapping dynamics of a single flag next to the wall at three typical gap clearances,  $G_c/W = 0.19, 0.31, \text{ and } 0.5$ , and the resultant heat transfer enhancement were first investigated to establish a benchmark. When  $G_c/W = 0.19$ , the clearance was equal to the flag

length, i.e.,  $G_c = L$ ; any further reduction in  $G_c$  would disturb the flapping motions of the flag because of the latent physical contact between the flag and the wall. When  $G_c/W = 0.5$ , the inverted flag was mounted along the centerline of the channel.  $G_c/W = 0.31$  was designed to keep the distance between the channel centerline and the flag at  $L$ , such that the two flags would not touch when configured side-by-side, as discussed in Section 3.2. Three distinct dynamic regimes, the biased, flapping, and deflected modes, were recognized with consecutive increases in the Reynolds number,  $Re_W$ , (indicating that the dimensionless bending stiffness  $K_B$  decreased), as shown in Fig. 4(a). No obvious wall confinement effect was observed on the flag flapping dynamics, and when  $G_c/W$  varied, the dynamic regimes remained almost unchanged, with a similar  $Re_W$  range. In biased mode (1), the flag mainly flapped asymmetrically to one side with moderate amplitudes of  $A/L = 0.7\text{--}1.2$  at  $Re_W = 1.64 \times 10^4\text{--}1.73 \times 10^4$ ; for the following experiments, the flag flapping amplitude  $A$  was defined as the maximum tip-to-tip displacement in transverse direction. The instantaneous motions of the inverted flag were recognized by a monitor point located  $0.8L$  (curvilinear distance along the flag) away from the trailing edge, as shown in Fig. 4(a). Fig. 4(b) gives a typical trajectory of the monitor point in the biased mode for  $G_c/W = 0.5$  and  $Re_W = 1.64 \times 10^4$ , showing a periodical flapping motion of the inverted flag restricted to a single side ( $x/L > 0$ ) with respect to the free state. In the flapping mode (2), a symmetric oscillation with a significant amplitude of nearly  $1.8L$  was identified for the  $Re_W$  range of  $1.81 \times 10^4$  to  $2.34 \times 10^4$ . The trajectory of the monitor point in the flapping mode approximated a sine-shaped curve (Fig. 4(c)). In the deflected mode (3), as  $Re_W$  increased further, the restoring bending force inside the flag was no longer comparable to the aerodynamic force exerted on the flag; therefore, the flag entirely deformed to the channel wall with a diminutive amplitude of less than  $0.2L$ , as shown in Fig. 4(d). These three dynamic regimes have been observed in previous studies [8,15,17], which also reported bi-stable states with small Reynolds number ranges in both the biased to flapping mode transitions and flapping to deflected mode transitions. In this study, the heat transfer experiments were conducted without the bi-stable states to avoid the effect of mode transition. In Fig. 4(b)–(d), dimensionless time is defined as  $\hat{t} = tU_0/L$ , where  $t$  denotes the physical time.

The additional turbulence was introduced by the energetic flapping flag, which facilitated the heat transfer enhancement from the heated plate. Yu et al. [15] reported that the channel turbulent kinetic energy can be locally elevated by over 80 times due to the presence of the flapping inverted flag. The performance of a single flag as a cooling mechanism across the three dynamic regimes has been widely investigated, using both numerical [16] and experimental [8,17] methods, and the results have consistently shown that an inverted flag in the flapping mode provides the best cooling performance among the three regimes. Consequently, this study quantified the heat transfer performance in the flapping mode. Fig. 5 depicts the contours of the distribution of the Nusselt number ratio,  $Nu^*$ , for  $G_c/W = 0.19$  (a and b),  $0.31$  (c and d), and  $0.5$  (e) at  $Re_W = 2.08 \times 10^4$ . The relative heat transfer enhancement performance indicated by the dimensionless Nusselt number was confirmed [8,17] to be insensitive to the Reynolds number in the flapping regime, as the flags' self-oscillating behaviors were similar. Thus, a moderate  $Re_W = 2.08 \times 10^4$  in the flapping mode was chosen as a representative demonstration. In addition, the poor dependency of the heat transfer performance on the Reynolds number is further clarified in Fig. 7. For  $G_c/W = 0.19$  and  $0.31$ , the inverted flag was mounted away from the centerline; in such configurations, the cooling performance of the near side and far side (wall sides 1 and 2, respectively, as shown in Fig. 1) should be measured individually. However, in this study's original experimental

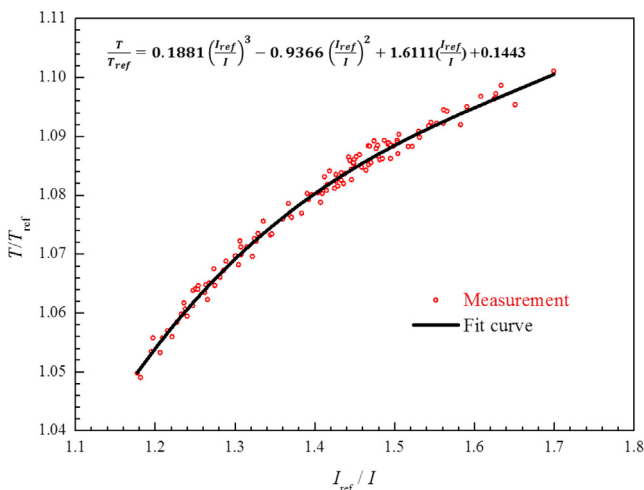
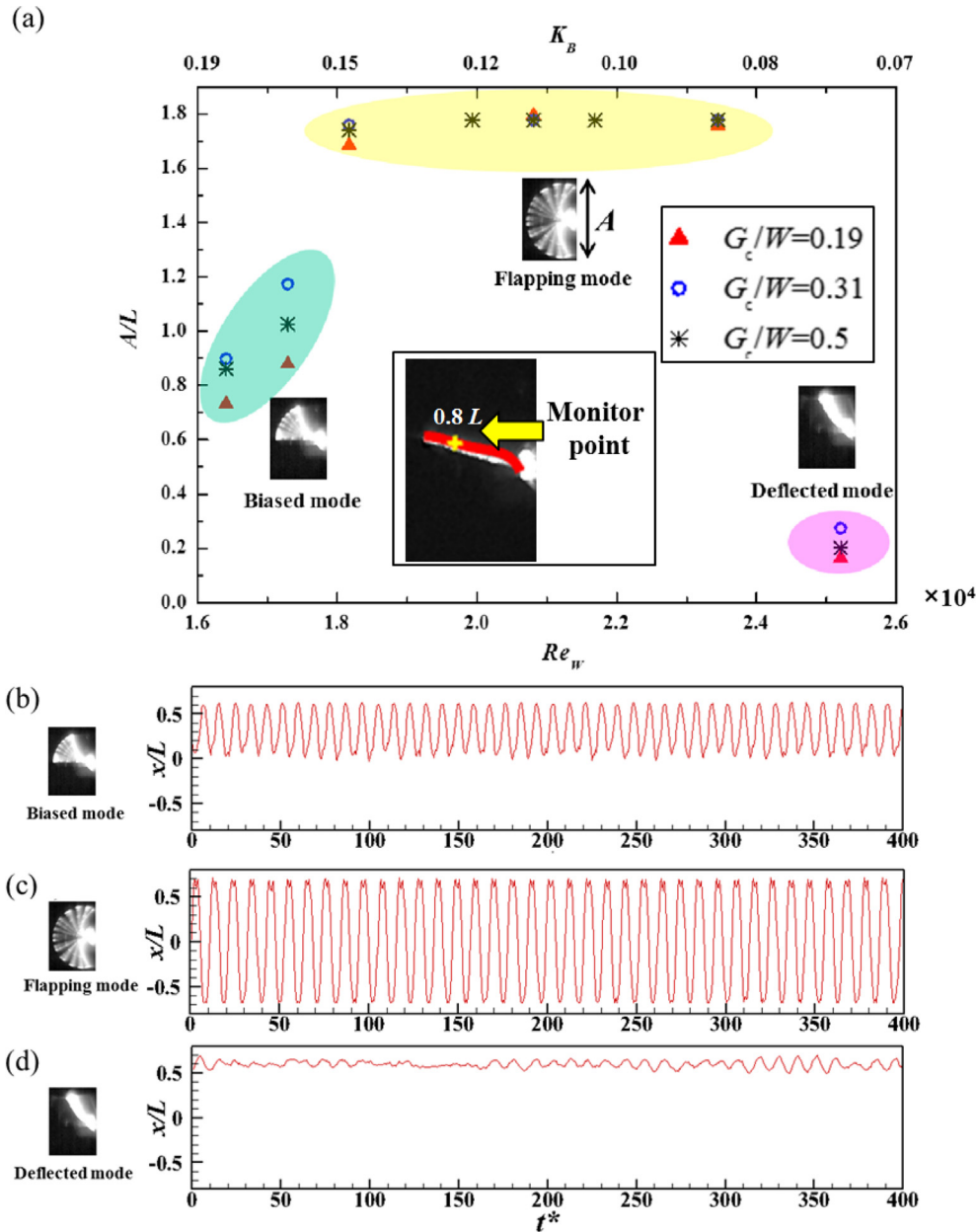


Fig. 3. In-situ calibration result for the TSP.



**Fig. 4.** Single flag dynamics: (a) dependency of the flapping amplitude and flapping dynamics on the Reynolds number,  $Re_w$ , and dimensionless bending stiffness,  $K_B$ , for various clearances  $G_c$ ; (b and d) trajectories of the monitor points for biased, flapping, and deflected modes, respectively.

set-up (Fig. 2), only wall side 1 with the heated plate was available for heat transfer measurements, while wall side 2 consisted of a transparent Plexiglas plate where the heat transfer was absent. To circumvent this issue, another experiment was conducted, with the inverted flag placed in the symmetric position along the centerline. For instance, the inverted flag mounted at  $G_c/W = 0.81$  was the counterpart for  $G_c/W = 0.19$ ; the heat transfer measured at side 1 for  $G_c/W = 0.81$  (Fig. 5(b)) could then be regarded as the result measured at side 2 for  $G_c/W = 0.19$ . The inverted flags along with their shadows are plotted as grey areas of various sizes in Fig. 5: for  $G_c/W = 0.19$ , side 1, (Fig. 5(a)), the inverted flag was far from the camera and LED source; accordingly the size of the blocked grey area is small. In contrast, for  $G_c/W = 0.81$ , side 1, (i.e.,  $G_c/W = 0.19$ , side 2, Fig. 5(b)), the inverted flag was close to the camera and LED source, so the grey area is enlarged.

Figs. 5 and 6 demonstrate that as the gap clearance between the inverted flag and the wall decreased,  $Nu'$  increased. Fig. 5(a) shows

that when  $G_c/W = 0.19$ ,  $Nu'$  increased remarkably to 1.5 for  $0.5 < Y^+ < 1.75$  at wall side 1 before gradually decreasing for  $Y^+ > 2$ . In contrast, Fig. 5(b) shows that the best cooling region shifted to  $2.5 < Y^+ < 4$ , with a  $Nu'$  value around 1.2 at side 2 (0.81 W away from the flag). The difference in cooling performance between wall sides 1 and 2 can be explained by the vortex shedding process that takes place behind the inverted flag. PIV measurements [7,15,17] and numerical studies [26] have confirmed that the shedding vortex emits toward the wall and transports downstream. The shedding vortex attached to wall side 1 was immediately behind the flag and swept out the thermal boundary layer, which significantly strengthened the heat transfer performance of the configuration with the small gap clearance  $G_c/W = 0.19$ . The spanwise-averaged  $Nu'$  distributions in Fig. 6 (red<sup>1</sup>

<sup>1</sup> For interpretation of color in Figs. 6, 9, 11 and 15, the reader is referred to the web version of this article.

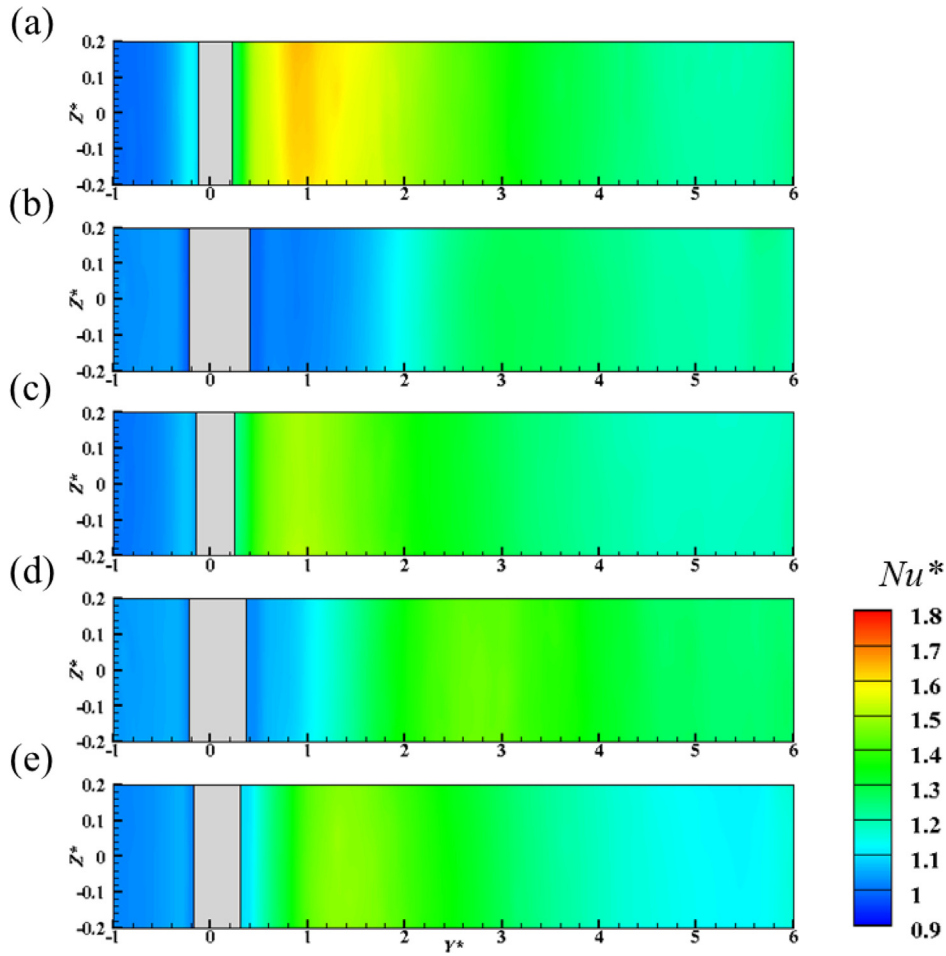


**Fig. 5.** Contours of the  $Nu^*$  distribution for a single flag at  $Re_W = 2.08 \times 10^4$ : (a and b)  $G_c/W = 0.19$ , wall sides 1 and 2, respectively; (c and d)  $G_c/W = 0.31$ , wall sides 1 and 2, respectively; (e)  $G_c/W = 0.5$ .

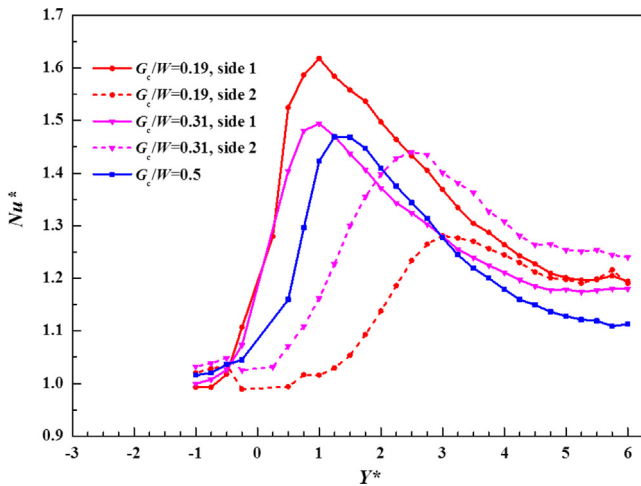


**Fig. 6.** Spanwise-averaged  $Nu^*$  distribution of a single flag with various  $G_c$  values at  $Re_W = 2.08 \times 10^4$ .

solid line) also showed that the maximum  $Nu^* = 1.6$  rose at  $Y^* = 1$ . As the flag was farther from wall side 2 (gap clearance  $0.81W$ ), the vortex dissipated and was transported downstream before attaching to the wall; the weaker peak  $Nu^* = 1.27$  then shifted downstream at  $Y^* = 3$  (Fig. 6, red dashed line). A similar phenomenon was observed for  $G_c/W = 0.31$  and  $0.5$ ; that is, as shown in Fig. 6, the maximum  $Nu^*$

was attenuated to  $1.5$  (purple solid line) at  $Y^* = 1$  when the inverted flag moved to  $G_c/W = 0.31$ . However, compared with the red dashed line ( $G_c/W = 0.19$ , side 2), the heat transfer performance for side 2 at  $G_c/W = 0.31$  was substantially augmented with an elevated  $Nu^*$  value exceeding  $1.4$  at  $Y^* = 2.5$ . When the inverted flag was mounted along the centerline for  $G_c/W = 0.5$ , the heat transfer performance on sides 1 and 2 should be the same, because the two walls are symmetric; consistent with this prediction, a moderate peak  $Nu^* = 1.46$  was obtained at  $Y^* = 1.5$ .

There was a heat transfer performance trade-off between the two walls: a larger  $Nu^*$  was achieved with a closer gap clearance,  $G_c$ , at side 1 due to the vigorous vortex shedding process from the inverted flag; however,  $Nu^*$  significantly declined because the shedding vortex dissipated before sweeping out the thermal boundary layer on wall side 2. To evaluate the comprehensive heat transfer performance of inverted flags with various  $G_c$  values, a thermal enhancement factor  $\eta$  [8,16,27,28] that accounted for both heat transfer benefit,  $\overline{Nu}/\overline{Nu}_0$ , and pressure drop penalty,  $F/F_0$ , was defined as follows:

$$\eta = \frac{\overline{Nu}/\overline{Nu}_0}{(F/F_0)^{1/3}}, \tag{5}$$

where  $\overline{Nu}$  is the global space-averaged Nusselt number for the two wall sides, subscript 0 denotes the smooth channel value at the corresponding Reynolds number,  $F = 2\Delta pW/L_h\rho_fU_0^2$  is the friction factor,  $\Delta p$  is the pressure drop between two pressure taps located at

$Y^* = -3.5$  and  $6$ ,  $L_h = 9.5W$  is the distance between the two pressure taps, and  $\rho_s$  is the air density. It is not reasonable to compare only the Nusselt number with that of the clean channel, because the channels modified with vortex generators such as flags and ribs always require more pumping power than a clean channel at the same Reynolds number. The thermal enhancement factor  $\eta$  is defined as the ratio of the Nusselt number of a modified channel to that of a smooth channel at a constant pumping power [27]. Eq. (5) allows a comparison between the clean channel and the modified channel. Table 1 summarizes the heat transfer performance and friction characteristics of the single inverted flag mode. The highest thermal enhancement factor of  $\eta = 1$  was achieved at  $G_c/W = 0.19$ , which is around 4% higher than that of  $G_c/W = 0.5$ . Placing the self-oscillating inverted flag in proximity to the channel wall improved the heat transfer performance.

The effect of the Reynolds number on heat transfer performance of the inverted flags is demonstrated in Fig. 7. Keeping the inverted flags in the flapping mode for  $G_c/W = 0.19$  in the  $Re_W$  range of  $1.81 \times 10^4 - 2.34 \times 10^4$  resulted in an almost unchanged spanwise-averaged  $Nu^*$  distribution for side 1, with a similar peak  $Nu^*$  value around 1.6 at  $Y^* = 1$ . For side 2, the maximum  $Nu^*$  slightly increased from 1.23 to 1.31 as the  $Re_W$  rose from  $1.81 \times 10^4$  to  $2.34 \times 10^4$ . It seems that the trends of  $Nu^*$  distributions are similar in the whole Reynolds number range of flapping regime, which is consistent with previous studies [8,17]. Accordingly,  $Re_W$  was kept at the fixed value of  $2.08 \times 10^4$  for the side-by-side and staggered flags systems, as described in the following sections.

### 3.2. Side-by-side flags

Promoting heat removal in the channel flow by placing a single inverted flag close to the wall had an inevitable disadvantage: the near wall (side 1) received sufficient cooling enhancement, but the far wall (side 2) had poor cooling. Placing two inverted flags side-by-side (Fig. 2(c)) seems to be an effective method for obtaining adequate heat transfer augmentation on both channel walls. Two typical gap clearances were investigated,  $G_c/W = 0.19$  and  $0.31$ , which tested distances between the two flags in the transverse direction of  $G_x/L = 3.33$  and  $2$ , respectively. Fig. 8 demonstrates that the flapping amplitude and dynamics of the side-by-side flags were dependent on  $K_B$  and  $Re_W$ . Comparing these with the single flag configurations, the three distinct dynamic regimes were located in similar  $Re_W$  ranges for the side-by-side configurations at  $G_c/W = 0.19$  and  $G_c/W = 0.31$ , but the transition  $Re_W$  between the biased, flapping, and deflected modes, declined slightly to  $1.73 \times 10^4$  and  $2.26 \times 10^4$ , respectively.

However, the flapping dynamics of the side-by-side inverted flags for  $G_c/W = 0.19$  and  $0.31$  were totally different. Fig. 9 depicts the snapshots of flag movement and the trajectories of the monitor points at  $Re_W = 2.08 \times 10^4$ . For  $G_c/W = 0.19$  (Fig. 9(a) and (b)), the two flags flapped in phase with periodic and synchronous motions; in contrast, the flapping motions for  $G_c/W = 0.31$  were chaotic (Fig. 9(c) and (d)), as the two flags alternately flapped toward one single side or both. For instance, flag 2 (Fig. 9(d), red line) flapped symmetrically at  $20 < t^* < 80$ , whereas it flapped toward a single side at  $0 < t^* < 230$ . Fig. 9(c) shows the profiles of the chaotic

**Table 1**  
Heat transfer performance and friction characteristics of single inverted flag for various  $G_c$ .

$G_c/W$	$\overline{Nu}/\overline{Nu}_0$	$F/F_0$	$\eta$
0.19	1.18	1.65	1.00
0.31	1.19	1.78	0.98
0.5	1.17	1.80	0.96

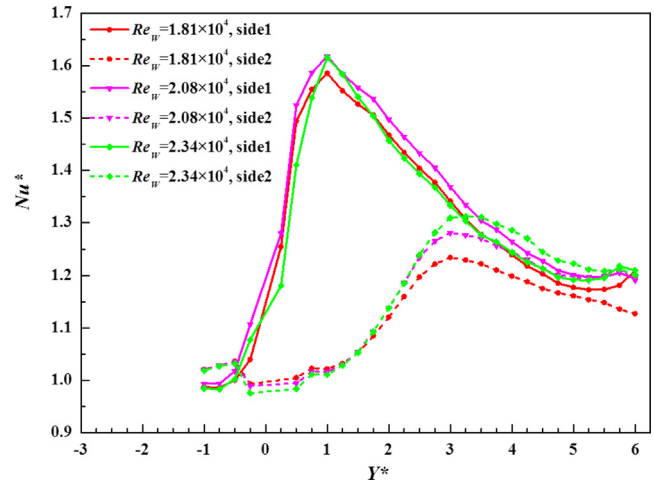


**Fig. 7.** Spanwise-averaged  $Nu^*$  distribution for a single flag with  $G_c/W = 0.19$  at various  $Re_W$  values.

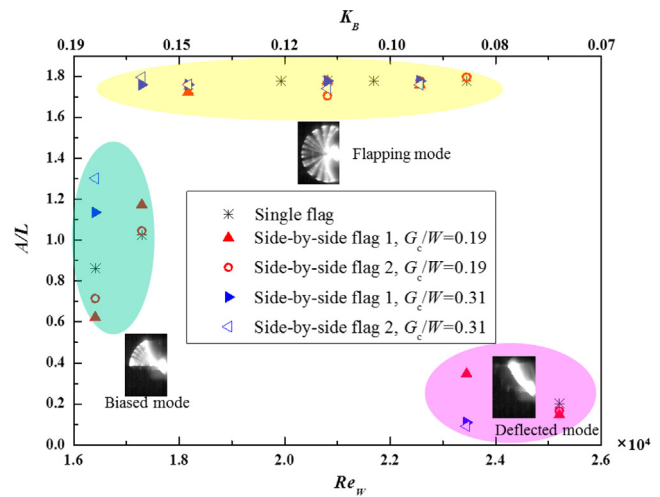


**Fig. 8.** Side-by-side flag dynamics. The flapping amplitude and dynamics depend on the Reynolds number,  $Re_W$ , and the dimensionless bending stiffness,  $K_B$ , for various gap clearances,  $G_c$ .

inverted flags at  $t^* = 0-20$ . Flag 1 flapped symmetrically, whereas flag 2 purely oscillated toward the bottom wall. Such irregular flapping motions were also observed experimentally by Huertas-Cerdeira et al. [18], and may be the result of strong interactions between the two flags.

Fig. 10 compares the  $Nu^*$  distributions of the side-by-side flags (Fig. 10(b) and (d)) with that of a single flag (Fig. 10(a) and (c)) at  $Re_W = 2.08 \times 10^4$ . Compared with the single inverted flag at  $G_c/W = 0.19$  (Fig. 10(a)), Fig. 10(b) shows a remarkable rise in  $Nu^*$  above 1.6 behind the side-by-side flags from  $Y^* = 0.75$  to  $2$ , which can be attributed to the additional turbulence caused by the second self-oscillating inverted flag. Furthermore, the peak  $Nu^*$  rose to 1.8 at  $Y^* = 1$  (Fig. 11, green line). As the side-by-side flags were close to the wall ( $G_c/W = 0.19$ ) and far from each other ( $G_x = 3.33L$ ), they still flapped with large amplitudes and symmetric motions, and the heat transfer performance, indicated by  $Nu^*$ , was significantly elevated. However, the results differed when the two side-by-side inverted flags were placed close to each other ( $G_x = 2L$ , i.e.,  $G_c/W = 0.31$ ). A diminutive elevation in  $Nu^*$  was observed in the side-by-side flags (Fig. 10(d)) compared to the single flag (Fig. 10(c)) for  $G_c/W = 0.31$ . The peak  $Nu^*$  slightly increased to 1.54 at  $Y^* = 1.25$  for the side-by-side inverted flags (Fig. 11, blue

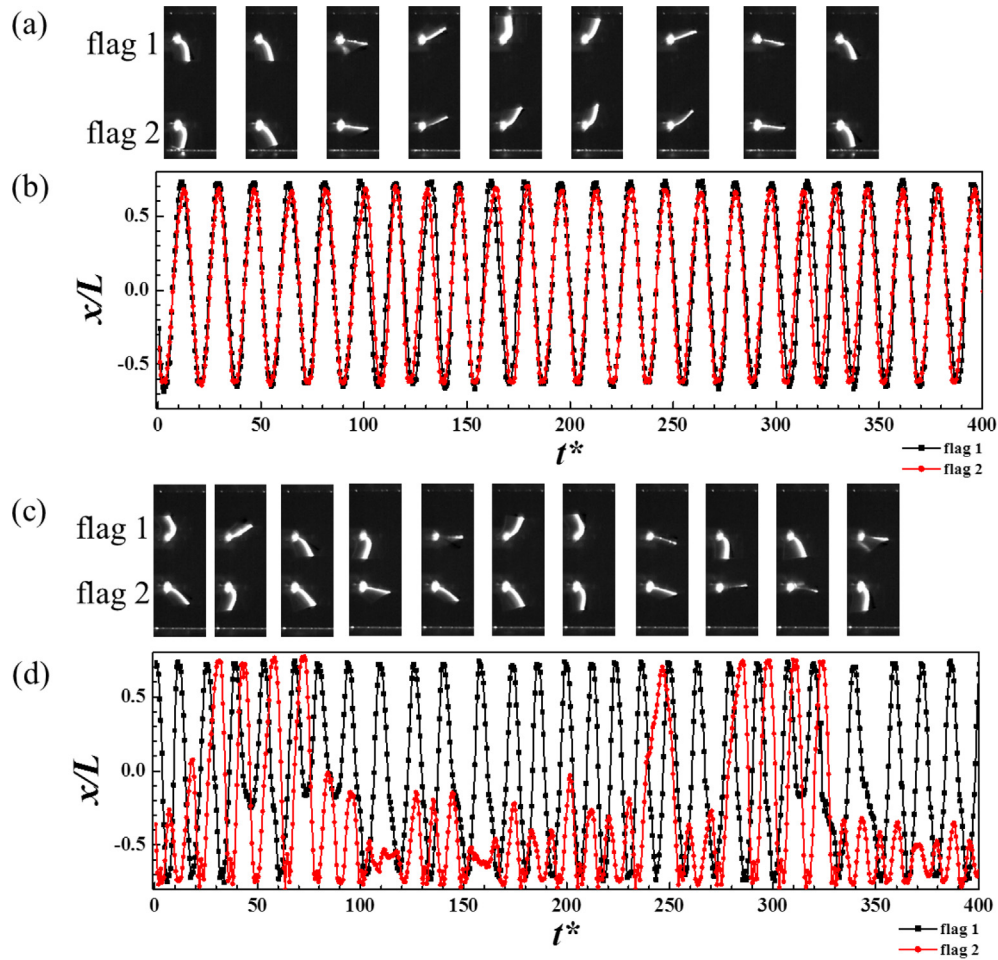


Fig. 9. Snapshots of the side-by-side flags and the trajectories of the monitor points: (a and b)  $G_c/W = 0.19$  and (c and d)  $G_c/W = 0.31$ .

line), a little higher than peak  $Nu^* = 1.49$  at  $Y^* = 1$  for the single inverted flag (Fig. 11, purple line). In addition,  $Nu^*$  for the side-by-side case was even smaller than for the single inverted flag at  $-0.25 < Y^* < 1$ . This small enhancement in heat transfer can be explained by the chaotic motions of the side-by-side flags at  $G_c/W = 0.31$ . At times, the side-by-side flags only flapped toward a single side with smaller amplitudes; therefore, the resulting turbulence of the surrounding fluid may be incomparable to that of symmetrically flapping flags.

Table 2 compares the heat transfer performance and friction characteristics of the side-by-side flags with those of the single inverted flag. For  $G_c/W = 0.19$ , the global averaged Nusselt number ratio,  $\overline{Nu}/\overline{Nu}_0$ , was augmented to 1.30 for the side-by-side configuration, and a benefit of around 10% was successfully achieved relative to the single flag ratio of  $\overline{Nu}/\overline{Nu}_0 = 1.18$ . However, the friction ratio,  $F/F_0$ , increased by 68% because of the additional flag's blockage, which overall reduced efficiency  $\eta$  by 7%. In contrast to the single inverted flag for  $G_c/W = 0.31$ ,  $\overline{Nu}/\overline{Nu}_0$  was enhanced by 3% for the side-by-side flags, and the  $F/F_0$  increased by approximately 70%, resulting in an uneconomic thermal enhancement efficiency of  $\eta = 0.86$ .

### 3.3. Staggered flags

The flapping dynamics and heat transfer characteristics of the staggered inverted flags were investigated. As the single flag and side-by-side flags configurations gave the best heat transfer

performance at  $G_c/W = 0.19$ , the gap clearance for the staggered flags was maintained at the same value. The separation distances in the streamwise direction were  $G_y/W = 2$  and 4, as shown in Fig. 1(d). The staggered flags' flapping dynamics and the resultant heat transfer performances were compared with those of the side-by-side flags, i.e.,  $G_y/W = 0$ . Fig. 12 shows that the flapping amplitude and flapping dynamics depended on the  $Re_W$  and  $K_B$  of the staggered inverted flags. For the staggered configurations  $G_y/W = 2$  and 4, the flapping amplitude and dynamic regimes were also similar to those of the single flag. The two staggered flags flapped synchronously with nearly the same amplitude throughout the entire  $Re_W$  range. For brevity, Fig. 12 only depicts the flapping amplitude of the front flag 1.

The trajectories of the monitor points revealed the time history of the flag motions for  $G_y/W = 0$  (side-by-side) and 2 and 4 (staggered), as shown in Fig. 13. For the side-by-side system  $G_y/W = 0$ , the two flags flapped symmetrically toward both sides with no phase delay. However, their dimensionless flapping period,  $\Delta t^*$ , remarkably increased from 10.9 (isolated single flag, Fig. 4(c)) to 16.4, indicating that the side-by-side flags oscillated more slowly than the single flag. As for the staggered systems  $G_y/W = 2$  and 4, Fig. 13(b) and (c), show that the two flags flapped in coupled motions with a constant phase delay and their flapping periods,  $\Delta t^*$ , recovered to around 10.4, which is comparable to the single flag value of  $\Delta t^* = 10.9$ . We can infer that the interactions between the staggered flags were weaker than those between the side-by-side flags. Therefore, placing the dual flags in a staggered configuration might eliminate the chaotic motions observed in the side-

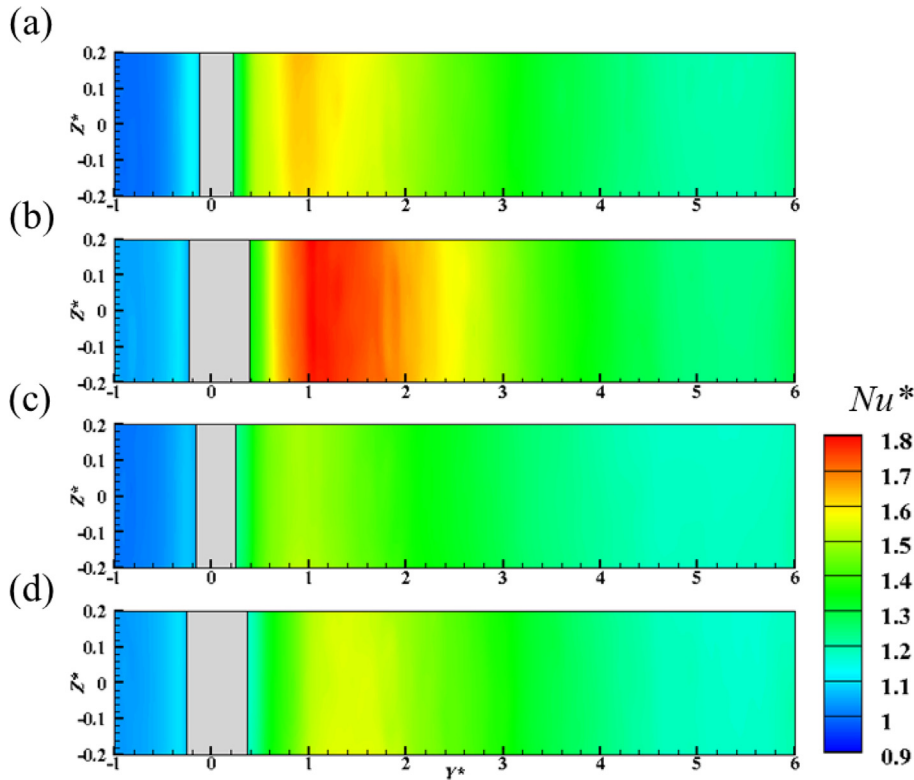


**Fig. 10.** Contours of the  $Nu^*$  distribution for various  $G_c$  values at  $Re_W = 2.08 \times 10^4$ : (a) single flag at  $G_c/W = 0.19$ , wall side 1; (b) side-by-side flags at  $G_c/W = 0.19$ ; (c) single flag at  $G_c/W = 0.31$ , wall side 1; and (d) side-by-side flags at  $G_c/W = 0.31$ .

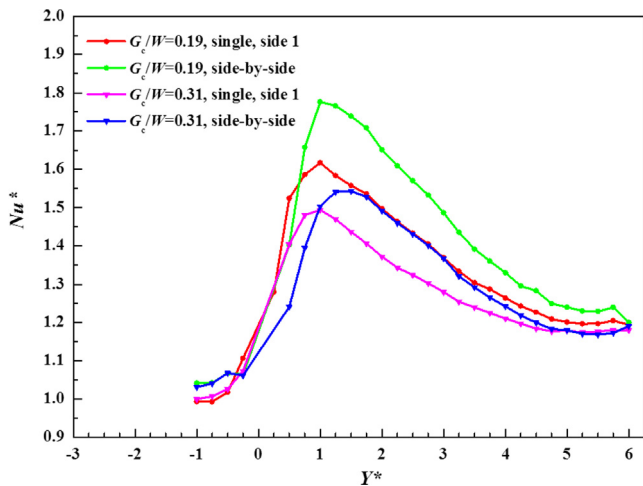


**Fig. 11.** Spanwise-averaged  $Nu^*$  distribution of the single flag and side-by-side flags for various  $G_c$  values at  $Re_W = 2.08 \times 10^4$ .

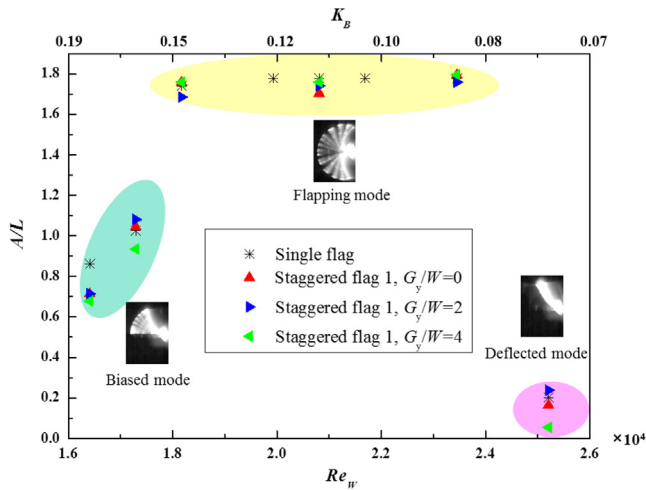
by-side system with close flag distances, which is a common configuration for narrow channels.

Fig. 14 plots the contours of the  $Nu^*$  distribution for the staggered flags at  $Re_W = 2.08 \times 10^4$ . For  $G_y/W = 2$ ,  $Nu^*$  quickly rose to 1.7 behind the front flag at  $Y^* = 0.6$  (Fig. 14(b)), with a peak value 1.65 at wall side 1, before the heat transfer performance decayed at  $Y^* > 1.7$ . Fig. 15 demonstrates that the spanwise-averaged  $Nu^*$  for the staggered flags was 0.15 higher (purple solid line,  $G_y/W = 2$ , wall side 1) at  $Y^* > 3.5$  than the single flag (red solid line). This can be attributed to the rear flag’s vigorous flapping motion. The  $Nu^*$  distribution was distinct at wall side 2 (Fig. 14(c)), as the cooling augmentation behind the front flag was almost ignorable

before  $Y^* = 1.8$ : the front flag was far from wall side 2 and the shedding vortex did not sweep out the thermal boundary layer at  $Y^* < 1.8$ . In addition, the rear flag was mounted in proximity to wall side 2, which gave the region  $2.2 < Y^* < 3.5$  favorable heat removal conditions, resulting in a high  $Nu^*$  value that exceeded 1.7. The peak  $Nu^*$  was observed at nearly 1.9 (Fig. 15, purple dashed line), which was even higher than that of the side-by-side configurations’  $Nu^* = 1.8$  (Fig. 15, blue solid line), perhaps because for a single inverted flag, the  $Nu^*$  peak was observed 1W and 3W downstream from the flag at wall sides 1 and 2, respectively, as shown in Fig. 6. Similarly, for the staggered system  $G_y/W = 2$ , the front flag was mounted at  $Y^* = 0$ , and the best cooling region was located at around  $Y^* = 3$  for wall side 2; the rear flag was mounted in proximity to wall side 2 at  $Y^* = 2$ , and its best cooling region was at about 1W behind the rear flag, i.e.,  $Y^* = 3$ . The concerted influence of the dual staggered flags substantially enhanced the heat removal performance, with a maximum  $Nu^*$  of around 1.9 at  $Y^* = 2.75$ , wall side 2. When the rear flag moved to  $Y^* = 4$  (Fig. 14 (d) and (e)), the heat transfer performance at side 1 was similar to that of  $G_y/W = 2$  (Fig. 14(b)); however, the peak  $Nu^*$  region for wall side 2 shifted downstream to  $4.4 < Y^* < 5$  (Fig. 14(e)). Table 3 indicates that the most economic cooling performance with a ther-

**Table 2**  
Heat transfer performance and friction characteristics of the side-by-side inverted flags for various  $G_c$  values.

Configuration	$G_c/W$	$\bar{Nu}/\bar{Nu}_0$	$F/F_0$	$\eta$
Single	0.19	1.18	1.65	1.00
Side-by-side	0.19	1.30	2.78	0.93
Single	0.31	1.19	1.78	0.98
Side-by-side	0.31	1.22	2.81	0.86



**Fig. 12.** Staggered flag dynamics: flapping amplitude and dynamics depend on the Reynolds number,  $Re_w$ , and the dimensionless bending stiffness,  $K_B$ , for various separation distances,  $G_y$ , at a fixed gap clearance of  $G_c/W = 0.19$ .

mal enhancement efficiency of  $\eta = 0.94$  was achieved at  $G_y/W = 2$ . In contrast to our previous study [8],  $\eta = 0.87$  was obtained by placing inverted flags ( $C^* = 0.25$ ) in tandem along the channel centerline with a similar Reynolds number. Accordingly, placing the shorter inverted flags ( $C^* = 0.19$ ) proximate to the wall in staggered configuration could further improve heat transfer performance.

**4. Conclusions**

This study investigated the flapping dynamics of dual self-oscillating inverted flags close to the walls within a turbulent channel flow in both side-by-side and staggered configurations. It examined the resultant heat transfer enhancement performance on the channel walls. The time varying curving profiles of the deformed inverted flags were chronologically recorded by a high-speed camera and then identified using a structure boundary detection algorithm. The heat transfer performance indicated by the Nusselt number ratio  $Nu^*$  was measured quantitatively using the TSP measurement technique.

Three distinct dynamic regimes based on the Reynolds number,  $Re_w$ , and the dimensionless bending stiffness,  $K_B$ , i.e., the biased, flapping, and deflected modes, were identified for a single inverted flag with gap clearances of  $G_c/W = 0.19, 0.31,$  and  $0.5$ . The wall confinement effect of the different gap clearances on the flapping dynamics was ignorable. The best heat transfer enhancement with  $\eta = 1.00$  was achieved when the flag was placed close to the channel wall with  $G_c/W = 0.19$ , and the maximum  $Nu^*$  of around 1.6 was observed at  $Y^* = 1$  for wall side 1 at  $Re_w = 2.08 \times 10^4$ . As the gap clearance increased and the flag was moved farther away from the wall to  $G_c/W = 0.5$ , the peak  $Nu^*$  region shifted downstream at  $Y^* = 1.5$  and the  $Nu^*$  value declined by 1.46. No obvious Reynolds number effect was found on the heat transfer performance in the flapping mode for the  $Re_w$  range from  $1.81 \times 10^4$  to  $2.34 \times 10^4$ .

Two inverted flags arranged in side-by-side configurations were subsequently studied. The same three dynamic regimes were

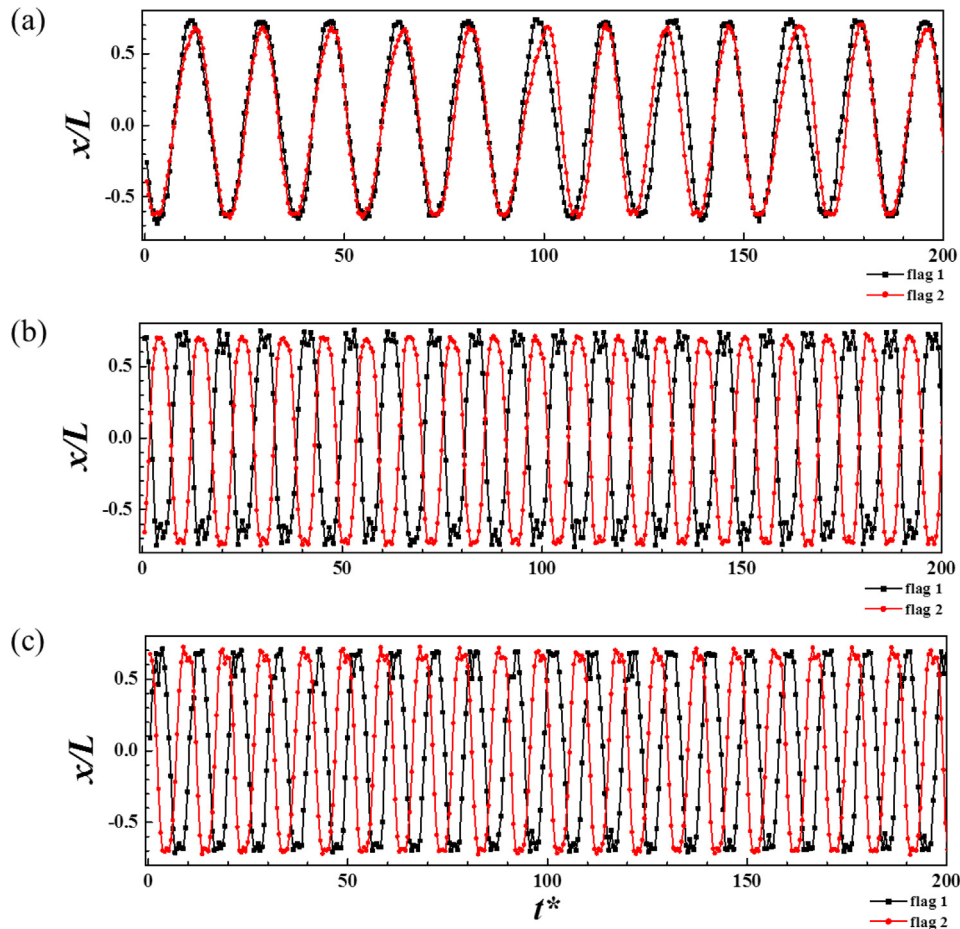


**Fig. 13.** Trajectories of the monitor points for the fixed gap clearance  $G_c/W = 0.19$  and various separation distances: (a–c)  $G_y/W = 0, 2,$  and  $4$ , respectively.

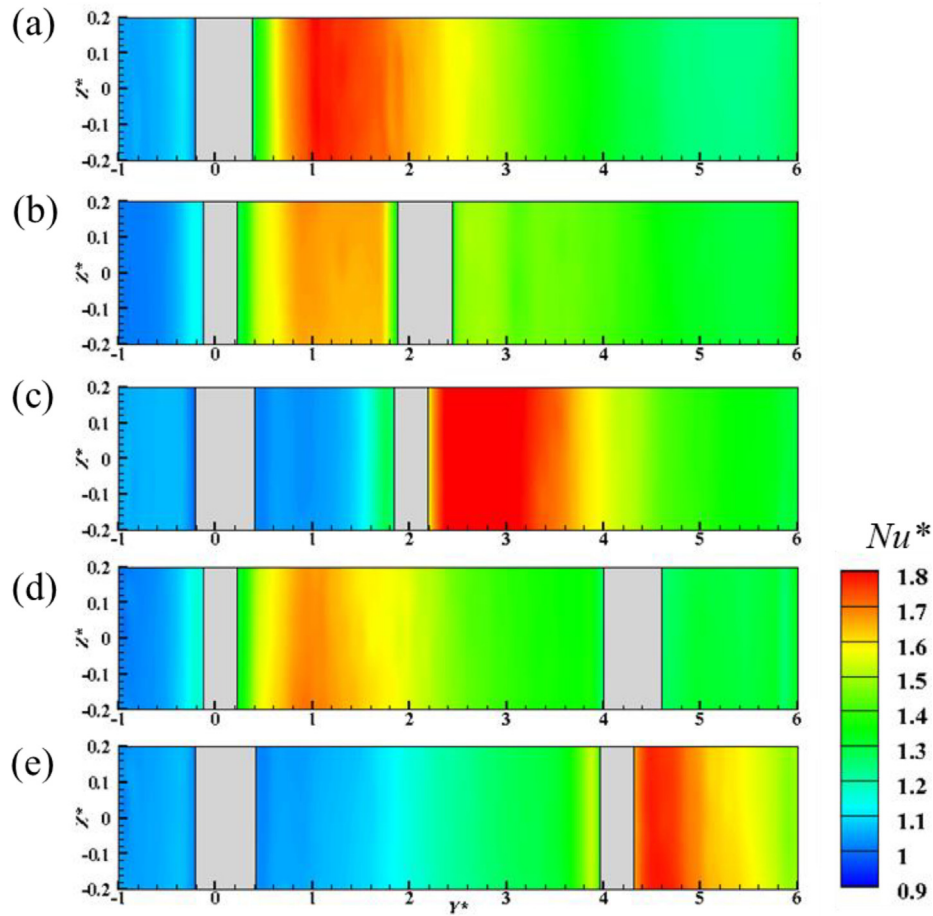


Fig. 14. Contours of the  $Nu^*$  distribution for staggered flags at  $Re_W = 2.08 \times 10^4$  and  $G_c/W = 0.19$ : (a)  $G_y/W = 0$ ; (b and c)  $G_y/W = 2$ , wall sides 1 and 2, respectively; (d and e)  $G_y/W = 4$ , wall sides 1 and 2, respectively.

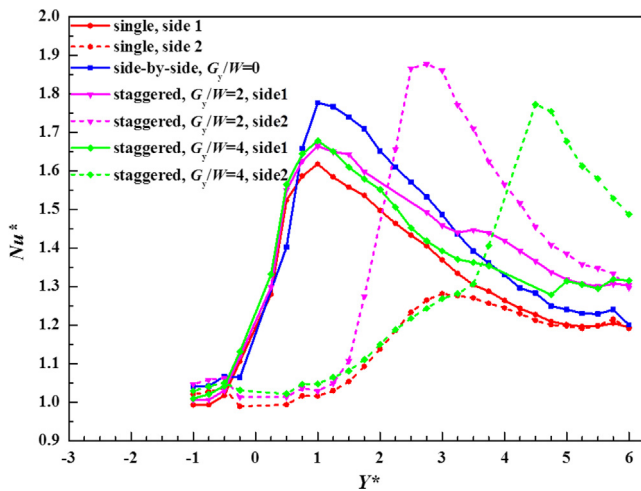


Fig. 15. Spanwise-averaged  $Nu^*$  distribution of staggered flags for various  $G_y$  values at  $Re_W = 2.08 \times 10^4$ .

examined. The two flags periodically and synchronously flapped with the same phase for  $G_c/W = 0.19$  at  $Re_W = 2.08 \times 10^4$ ; however, the dimensionless flapping period increased to  $\Delta t^* = 16.4$ , much longer than for the isolated single flag  $\Delta t^* = 10.9$ . In contrast to the single flag with  $G_c/W = 0.19$ , an elevated maximum  $Nu^* = 1.8$  was recognized at  $Y^* = 1$  for the side-by-side flags with

Table 3

Heat transfer performance and friction characteristics of the staggered inverted flags for various  $G_y$  at  $G_c/W = 0.19$ .

$G_y/W$	$\overline{Nu}/\overline{Nu}_0$	$F/F_0$	$\eta$
0	1.30	2.78	0.93
2	1.29	2.61	0.94
4	1.24	2.47	0.91

$G_c/W = 0.19$ . Although the global averaged Nusselt number ratio,  $\overline{Nu}/\overline{Nu}_0$ , rose to 1.30, the friction factor ratio,  $F/F_0$ , simultaneously increased by 68%, which led to an overall downward trend in thermal enhancement efficiency of  $\eta = 0.93$ . As for  $G_c/W = 0.31$ , the two side-by-side flags were closer to each other, resulting in chaotic flapping motions: the two inverted flags alternated between a symmetric flapping motion toward both wall sides and an asymmetric flapping motion toward a single side.  $\overline{Nu}/\overline{Nu}_0 = 1.22$  was slightly augmented by 3% for the side-by-side flags with  $G_c/W = 0.31$ ; however,  $F/F_0$  was augmented by 70% due to the large blockage of the two flags, which eventually led to a significant decrease in thermal enhancement efficiency of  $\eta = 0.86$ .

The two staggered flags' coupling flapping behaviors were determined at  $Re_W = 2.08 \times 10^4$  for  $G_y/W = 2$  and 4. Unlike the side-by-side system, the oscillating dynamics of the staggered flaps was similar to that of the single flag, i.e., with a comparable flapping period  $\Delta t^* = 10.4$  and amplitude  $A/L = 1.8$ . The maximum heat transfer enhancement  $Nu^* = 1.9$  was achieved at  $Y^* = 2.75$ , which could be attributed to the concerted influence of two staggered

flags for  $G_y/W=2$ . The resultant thermal enhancement efficiency  $\eta = 0.94$  was superior to  $\eta = 0.87$ , which was obtained by mounting tandem flags along the channel centerline [8]. This shows that placing flags close to the wall in a staggered configuration is more economical than the single flag and side-by-side double flag configurations.

### Conflict of interest

The authors declare that they have no conflict of interest in relation to this study.

### Acknowledgments

The authors gratefully acknowledge financial support for this study from the National Natural Science Foundation of China (11725209).

### Appendix A. Supplementary material

Supplementary data to this article can be found online at <https://doi.org/10.1016/j.ijheatmasstransfer.2019.03.048>.

### References

- [1] J. Han, J.S. Park, Developing heat transfer in rectangular channels with rib turbulators, *Int. J. Heat Mass Transf.* 31 (1) (1988) 183–195.
- [2] G.J. VanFossen, Heat transfer coefficients for staggered arrays of short pin fins, ASME 1981 International Gas Turbine Conference and Products Show, American Society of Mechanical Engineers, 1981.
- [3] P. Ligrani, N. Burgess, S. Won, Nusselt numbers and flow structure on and above a shallow dimpled surface within a channel including effects of inlet turbulence intensity level, *J. Turbomach.* 127 (2) (2005) 321–330.
- [4] G.I. Mahmood, M.Z. Sabbagh, P.M. Ligrani, Heat transfer in a channel with dimples and protrusions on opposite walls, *J. Thermophys. Heat Transf.* 15 (3) (2001) 275–283.
- [5] H.-Y. Li, Y.-X. Wu, Heat transfer characteristics of pin-fin heat sinks cooled by dual piezoelectric fans, *Int. J. Therm. Sci.* 110 (2016) 26–35.
- [6] H. Ma, L. Tan, Y. Li, Investigation of a multiple piezoelectric–magnetic fan system embedded in a heat sink, *Int. Commun. Heat Mass Transf.* 59 (2014) 166–173.
- [7] D. Kim et al., Flapping dynamics of an inverted flag, *J. Fluid Mech.* 736 (2013).
- [8] Y. Chen et al., Heat transfer enhancement of turbulent channel flow using tandem self-oscillating inverted flags, *Phys. Fluids* 30 (7) (2018) 075108.
- [9] J.B. Lee, S.G. Park, H.J. Sung, Heat transfer enhancement by asymmetrically clamped flexible flags in a channel flow, *Int. J. Heat Mass Transf.* 116 (2018) 1003–1015.
- [10] J.B. Lee et al., Heat transfer enhancement by flexible flags clamped vertically in a Poiseuille channel flow, *Int. J. Heat Mass Transf.* 107 (2017) 391–402.
- [11] Y. Jin et al., On the couple dynamics of wall-mounted flexible plates in tandem, *J. Fluid Mech.* 852 (2018).
- [12] K. Shoele, R. Mittal, Computational study of flow-induced vibration of a reed in a channel and effect on convective heat transfer, *Phys. Fluids* 26 (12) (2014) 127103.
- [13] Y. Yu, Y. Liu, Flapping dynamics of a piezoelectric membrane behind a circular cylinder, *J. Fluids Struct.* 55 (2015) 347–363.
- [14] M. Shelley, N. Vandenberghe, J. Zhang, Heavy flags undergo spontaneous oscillations in flowing water, *Phys. Rev. Lett.* 94 (9) (2005) 094302.
- [15] Y. Yu, Y. Liu, Y. Chen, Vortex dynamics behind a self-oscillating inverted flag placed in a channel flow: time-resolved particle image velocimetry measurements, *Phys. Fluids* 29 (12) (2017) 125104.
- [16] S.G. Park et al., Enhancement of heat transfer by a self-oscillating inverted flag in a Poiseuille channel flow, *Int. J. Heat Mass Transf.* 96 (2016) 362–370.
- [17] Y. Yu, Y. Liu, Y. Chen, Vortex dynamics and heat transfer behind self-oscillating inverted flags of various lengths in channel flow, *Phys. Fluids* 30 (4) (2018) 045104.
- [18] C. Huertas-Cerdeira, B. Fan, M. Gharib, Coupled motion of two side-by-side inverted flags, *J. Fluids Struct.* 76 (2018) 527–535.
- [19] J. Ryu, S.G. Park, H.J. Sung, Flapping dynamics of inverted flags in a side-by-side arrangement, *Int. J. Heat Fluid Flow* 70 (2018) 131–140.
- [20] H. Huang, H. Wei, X.-Y. Lu, Coupling performance of tandem flexible inverted flags in a uniform flow, *J. Fluid Mech.* 837 (2018) 461–476.
- [21] T. Liu, *Pressure-and Temperature-Sensitive Paints*, Wiley Online Library, 2005.
- [22] C. He et al., Measurement of flow structures and heat transfer behind a wall-proximity square rib using TSP, PIV and split-fiber film, *Exp. Fluids* 57 (11) (2016) 165.
- [23] D. Peng et al., Simultaneous PSP and TSP measurements of transient flow in a long-duration hypersonic tunnel, *Exp. Fluids* 57 (12) (2016) 188.
- [24] Z. Ghorbani-Tari, Y. Chen, Y. Liu, End-wall heat transfer of a rectangular bluff body at different heights: temperature-sensitive paint measurement and computational fluid dynamics, *Appl. Therm. Eng.* 122 (2017) 697–705.
- [25] R.J. Moffat, Describing the uncertainties in experimental results, *Exp. Therm. Fluid Sci.* 1 (1) (1988) 3–17.
- [26] J. Ryu et al., Flapping dynamics of an inverted flag in a uniform flow, *J. Fluids Struct.* 57 (2015) 159–169.
- [27] P. Promvong, C. Thianpong, Thermal performance assessment of turbulent channel flows over different shaped ribs, *Int. Commun. Heat Mass Transf.* 35 (10) (2008) 1327–1334.
- [28] R.K.B. Gallegos, R.N. Sharma, Flags as vortex generators for heat transfer enhancement: gaps and challenges, *Renew. Sustain. Energy Rev.* 76 (2017) 950–962.